Geophysical Journal International

Geophys. J. Int. (2010) **181,** 951–965 doi: 10.1111/j.1365-246X.2010.04547.x

The dynamics of the 2001 Etna eruption as seen by full moment tensor analysis

A. Saraò,[1] O. Cocina,[2] E. Privitera[2] and G. F. Panza[3,4]

[1] *Istituto Nazionale di Oceanografia e di Geofisica Sperimentale, Centro Richerche Sismologiche, Trieste, Italy. E-mail: asarao@inogs.it*
[2] *Istituto Nazionale di Geofisica e Vulcanologia, Sezione di Catania, Italy*
[3] *Dipartimento di Scienze della Terra, Università degli Studi di Trieste, Trieste, Italy*
[4] *The Abdus Salam International Centre for Theoretical Physics, Trieste, Italy*

Accepted 2010 January 27. Received 2010 January 27; in original form 2009 January 26

SUMMARY

The Mt. Etna eruption of July 2001 was announced by severe seismic activity and by the opening of a 7-km-long zone of densely distributed fractures. The large amount of data collected gave a unique opportunity to study the magma migration process and to infer the position and geometry of the uprising dyke. Results from multidisciplinary approaches suggest that the observed phenomenology was the result of the rapid intrusion of a vertical dyke, oriented roughly N–S and located a few km south of the summit region.

To add new constraints to the dynamics of the eruption process, in this study we determine the full seismic moment tensors of 61 earthquakes, selected among those occurring between July 12 and July 18 ($M_d \geq 2.2$), located in a depth ranging from 1 km above sea level (a.s.l.) to 3 km below sea level (b.s.l.).

At the beginning of the seismic swarm, the dominant component of the seismic source tensor is double-couple percentage (around 65 per cent on average) statistical significant at 95 per cent confidence level and in the following hours the non-double-couple components increase at the expenses of the double-couple. Such observations are related well with the system of fractures formed just before the eruption, whereas the increasing non-double-couple components can be explained as the response of the confining rocks to the rising magma and degassing processes.

The type of focal mechanisms retrieved are predominantly of normal fault type (44 per cent), strike slip (30 per cent) and thrust mechanisms (9 per cent), and outline a scenario that concurs with the stress regime induced by a dyke injection.

The space–time analysis of seismic source locations and source moment tensors (1) confirms the evidence of a vertical dyke emplacement that fed the 2001 lateral eruption and (2) adds new insights to support the hypothesis of the injection of a second aborted dyke, 2 km SE from the fractures zone.

Key words: Time series analysis; Earthquake source observations; Volcano seismology; Eruption mechanisms and flow emplacement; Volcano monitoring.

1 INTRODUCTION

Between 2001 July 12 and 18, a seismic swarm of 2645 earthquakes was recorded by Istituto Nazionale di Geofisica e Vulcanologia, Sezione di Catania (INGV-CT) permanent seismic network and led to one of the most important flank eruptions in recent centuries. The swarm preceded and accompanied the opening of a 7-km-long system of fissures along the western rim of Valle del Bove (Patanè *et al.* 2002); it therefore proved a great opportunity to study the process of magma migration before the eruption started on July 17.

The 2001 Mt. Etna eruption began from the uppermost sector of the N–S trending fracture system with five vents opening at an altitude higher than 2600 m a.s.l. On July 18, a fissure opened at 2100 m (Monti Calcarazzi vent) and the following day two pit craters opened at 2550 m a.s.l. and gave rise to an intense explosive activity that in a few days formed the "Laghetto" cinder cone. The eruption ended on 2001 August 9 after the volcano had ejected a lava volume of approximately 48 million m^3 (INGV 2001). Petrological data (Corsaro *et al.* 2007) and geochemical analysis (Aiuppa *et al.* 2002) highlighted that two distinct volumes of magma fed the uppermost

fissure systems (higher than 2600 m a.s.l.) and the vents opened at 2550 and 2100 m.

The seismic swarm occurring before the eruption has been interpreted as the fragile response of the confining medium to the local stress field, generated by the final emplacement of a dyke during the first 48–72 hr of the seismic activity. The earthquake distribution, the hypocenter migration, the orientation of the *P*-axes at the source (Musumeci *et al.* 2004), the anomalous region of very low Q_p values (Martinez-Arevalo *et al.* 2005) together with other seismological evidence (Patanè *et al.* 2002, 2003; Behncke & Neri 2003; Alparone *et al.* 2004) and geodetic measurements (Bonaccorso *et al.* 2002, 2004) suggest that the 2001 flank eruption was fed by a near vertical dyke, oriented roughly N–S, located a few km south of the summit region.

The dyke emplacement took place in a different way to previous eruptions modelled in the last 20 years, which have generally shown shallow fracturing and radial propagation from the craters area, usually along preferential directions (Bonaccorso *et al.* 2002).

At the beginning of the seismic swarm, all the monitoring activities on the volcano were intensified and the databases obtained as a whole enable classifying the 2001 eruption as one of the best-monitored events at Mt. Etna volcano. The main feeding mechanism just described is consistent with almost all the observations made, but seismic activity (Patanè *et al.* 2002; Musumeci *et al.* 2004), gravity observations (Carbone *et al.* 2003), GPS measurements (Bonforte *et al.* 2004) and extensometer data (Gambino 2004) highlight a complex behaviour that cannot be explained by one simple intrusion mechanism, because all the geophysical information also points to important phenomena in a volume located 2–3 km SE from the eruptive scenario.

In this study, we investigate the source process of a selection of earthquakes occurring mainly during the early hours of the seismic swarm forerunning the 2001 eruption, with the aim of providing new insights into the eruption dynamics.

2 MOMENT TENSOR FROM WAVEFORM INVERSION

Knowing the earthquake source process can add new and stringent evidence to volcano dynamics, but to retrieve the full source moment tensor is a difficult task due to the small magnitude of the events and to the presence of both ambient noise (near villages) and volcanic tremor (in the upper part of the volcano). In this study, we use short-period seismograms to investigate the seismicity forerunning the 2001 eruption using the INPAR (INdirect PARameterization) method, as developed by Šílený & Panza (1991), Šílený *et al.* (1992) and Šílený (1998). The method consists of two main steps. In the first step (linear), the six moment rate functions (MTRFs), which describe a point source with a mechanism varying in time, are obtained after extracting the base functions from the data. The base functions—the medium response to a seismic source modelled by an elementary single source with the time dependence given by Heaviside function—are computed by the modal summation technique (e.g. Panza 1985; Panza *et al.* 2000), placing the source on a grid centred around the hypocentral depth estimate, and using two structural models, assumed to envelop the range of variability of the possible models of the study area. The base functions corresponding to hypocenter locations and structures not coinciding with a grid node are obtained by linear interpolation between the base functions computed at the relevant grid nodes. The synthetic seismogram, corresponding to a given source depth and structural model, is compared with the observed records and the difference computed through the L_2 norm that, minimized by a damped least-squares technique, supplies the best MTRFs which is the solution of the first step of the inversion.

In the second step, following the assumption that for weak events the focal mechanism is constant in time, we factorize the MTRFs into a constant moment tensor and a common source time function (STF). This entails extracting the source time function as a common part of the MTRFs and to retrieve the six moment tensor components of the average source mechanism. We adopt the parameterization of the MTRFs by means of a set of N triangles overlapping in their half width (Nabelek 1984). The decomposition of the MTRFs is a non-linear problem and is solved by imposing constraints such as positivity of the STF (i.e. only forward slips) and the requirement of a mechanism consistent with clear readings of first-arrival polarities. Considering the MTRFs as independent functions during the inversion leads to an overparametrization of the problem, which is advantageous for reducing the effects of poor modelling of the structure, whereas the subsequent decomposition of the MTRFs reduces the bias due to non-exact base functions because it keeps only their common part (Kravanja *et al.* 1999).

The reliability of the solutions is checked through error analysis that takes into account the errors due to the noise in the data and to an improper modelling of the base functions (ill-modelled structural features).

The moment tensor is decomposed into the volumetric (V) part representing volume changes, the compensated linear vector dipole (CLVD) part, which can be related to lenticular crack activation accompanied by possible fluid motion, and the double-couple (DC) part due to dislocation movements (Jost & Hermann 1989).

Following Guidarelli *et al.* (2002, 2006), we quantify the percentage of the moment tensor components using the scalar seismic moment relation $M_{tot}^2 = M_{dev}^2 + M_{iso}^2$ (Silver & Jordan 1982), where M_{tot} is the total seismic scalar moment, M_{dev} and M_{iso} are the deviatoric and the isotropic seismic moments, respectively. The deviatoric moment is obtained as the sum of the DC and CLVD seismic moment. The percentage of the deviatoric part is then computed as $(M_{dev}^2/M_{tot}^2) \times 100$ whereas $(M_{iso}^2/M_{tot}^2) \times 100$ gives the percentage of the V component. The information content of this formalism is equivalent to that of the representation adopted by Saraò *et al.* (2001).

Several papers have already discussed the limits and possibilities of the INPAR approach (e.g. Šílený *et al.* 1996; Panza & Saraò 2000; Saraò *et al.* 2001; Guidarelli & Panza 2006) mainly when studying short period data in complex environments. Synthetic tests have studied the influence of random noise, of the number of records employed, of modelling inconsistencies due to wave propagation effects or ill-modelled structural features (e.g. Šílený *et al.* 1992, 1996; Panza & Saraò 2000) on the solutions and how it is possible to discriminate between spurious non-double-couple and physically meaningful solutions. Applying the INPAR method, Saraò *et al.* (2001) studied the full moment tensor of a selected set of earthquakes that were forerunners of the 1991–1993 Etna eruption. For each investigated event, they performed systematic stability tests on the inversion results, and considered different time and frequency windows of records, different size of the search parameter grid, as well as different groups of stations to ascertain the presence of any significant variation in the solutions due to path properties or to the nodal position of the stations that might bias their interpretation. They demonstrated that scattering and reverberation effects could effectively be minimized by a proper application of INPAR

procedure and proved the robustness of the focal mechanism retrieved, in particular of the non-DC components found.

3 DATA AND ANALYSIS

From July 12 (at 21:44 UTC) until the end of the eruption, the INGV-CT seismic network (Fig. 1) recorded a total of 2694 earthquakes with $M \geq 1$. Most of the seismicity (2645 earthquakes) occurred before the eruptive event that began during the night between July 16 and July 17 with lava flow and fire fountains from the Mt. Etna South East Crater (Corsaro *et al.* 2007). The seismic energy released was relatively low and only 62 events had $M \geq 3.0$, the highest magnitude being 3.9 (Patanè *et al.* 2003).

Due to the presence of high tremor amplitude and of coda waves from previous events, which masked the first *P*-wave arrivals, only a part of the recorded seismicity was well located. The epicentral distribution (Patanè *et al.* 2002) shows a marked clustering, aligned in an N–S direction, to the South of the central craters area, along the main eruptive fracture system and a minor one located to the south-east, also oriented N–S.

We selected a data set of 61 events, belonging to the two identified clusters (Table 1), that satisfy the following constraints in the localization errors: horizontal error (erh) and vertical error (erz) less than 1 km, maximum angular separation between recording stations (gap) less than 120°, root mean square of residual times (r.m.s.) less than 0.3 s. These events, whose average r.m.s. has been estimated equal to 0.12 s, using the standard routine HYPOELLIPSE (Lahr 1989), have been relocated using SIMULPS12 code (Thurber 1993) and the 3D velocity model (Patanè *et al.* 2006) defined for the uppermost 7 km of the crust under Mt. Etna. The 3D relocations (Table 1) reduce the average r.m.s. from 0.12 to 0.07 s and the errors are 0.1 km in depth and 0.09 km along the horizontal direction.

The relocated events are evidently clustered at shallow depth and still grouped into the two main zones aligned in the N–S direction (Fig. 2); hereafter, we refer to the events located just beneath the surface fractures as Z1, and the events located to the southeast of Z1 as Z2 (Fig. 2).

The Z1 earthquakes, occurring between July 12 and July 18, with $1.6 \leq M_d \leq 3.5$, are deeper than 1 km a.s.l. and their alignment clearly indicates the position of the dyke injection as already pointed out by several authors (e.g. Musumeci *et al.* 2004). The Z2 events, recorded between July 13 and 15, with $2.3 \leq M_d \leq 3.5$, show a similar configuration and their hypocenters are located at sea level or deeper. The bottom of the seismogenic zone is at about 3.0 km b.s.l. for both clusters.

For each earthquake, we exclude noisy records, unsuitable for standard processing and data for which the epicentral distance is too small compared to the hypocentral depth. The latter condition is necessary for a straightforward application of the modal-summation

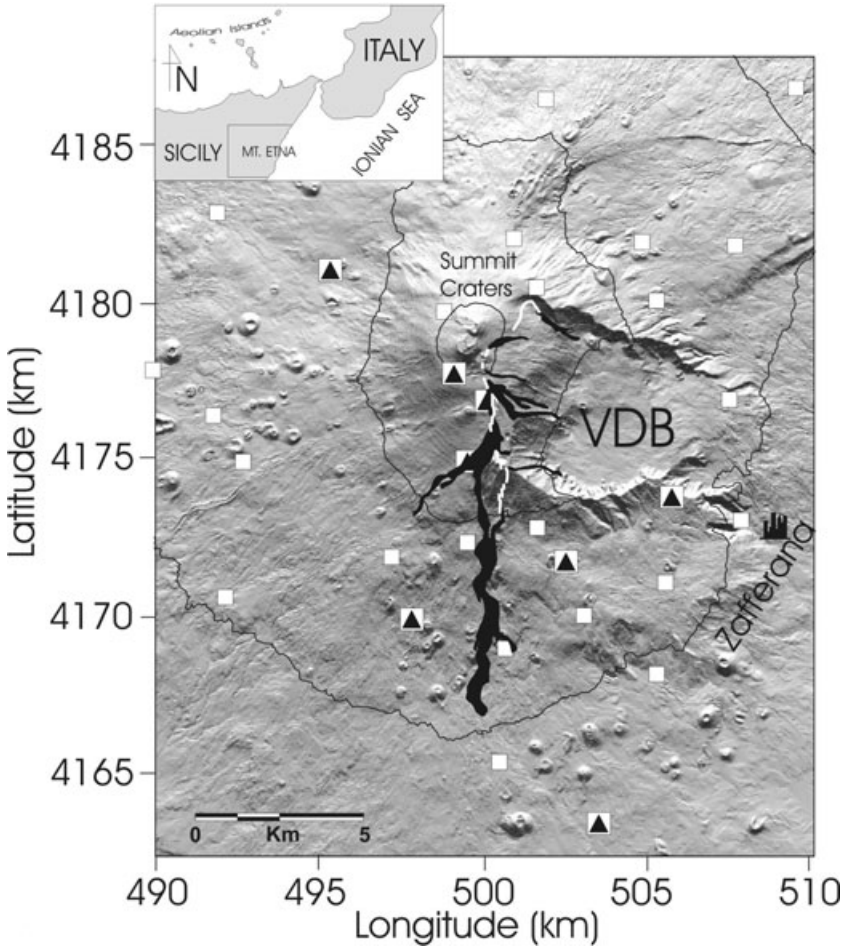

Figure 1. Map of the eruptive scenario of the 2001 eruption: fractures opened between July 12 and 17 (white lines) and lava flows (black stripes) are drawn. VDB indicates the Valle del Bove Caldera. The seismic stations (white squares: 1-component stations; black triangles: 3-component stations) located in the central part of the volcano and managed by the permanent INGV-CT network (Patanè *et al*. 2003) are also plotted.

Table 1. Focal parameters and results from the moment tensor inversion for the 61 earthquakes analysed in this study.

N	Day	hhmm	ss.ss	Lat.	Long.	Depth	Depth MT	M_d	M_w	M_o (Nm)	Corr	Str	Dip	Rake	FPS type	DC per cent	CLVD per cent	V per cent
1	10 712	2234	13.87	37.740	15.001	0.4	−0.04	2.3	2.9	2.90E+13	0.6	278	64	0	SS	74	7	19
2	10 712	2250	48.95	37.720	15.009	1.2	0.8	2	2.5	6.40E+12	0.5	182	76	113	TF	81	8	11
3	10 712	2315	29.02	37.724	15.007	1.5	1.6	2.6	2.5	7.30E+12	0.6	141	26	−171	UN	55	29	17
4	10 712	2332	14.62	37.722	15.011	1.1	1.9	2.4	2.9	2.60E+13	0.7	242	27	−163	UN	56	34	9
5	10 712	2333	10.17	37.722	15.010	0.3	2	2.4	2.5	5.60E+12	0.4	326	70	−45	NS	77	6	17
6	10 712	2339	54.21	37.741	15.007	0.2	0.9	2.3	2.1	1.70E+12	0.5	214	90	−111	UN	73	21	6
7	10 712	2347	43.93	37.719	15.010	1.0	0.4	2.2	2.5	6.30E+12	0.5	302	80	146	SS	73	5	22
8	10 712	2358	30.32	37.719	15.012	1.0	1.9	2.2	2.5	7.20E+12	0.5	190	74	−88	NF	55	35	10
9	10 713	0000	53.6	37.741	15.002	0.1	−0.3	1.6	2	1.00E+12	0.5	224	61	−107	NF	51	46	3
10	10 713	0003	10.31	37.720	15.010	2.6	3.3	2.3	3.1	4.30E+13	0.5	335	40	−160	NS	26	50	25
11	10 713	0006	16.66	37.744	15.000	0.5	−0.8	2.2	2	1.00E+12	0.8	59	61	−61	NF	60	8	32
12	10 713	0007	28.02	37.724	15.008	0.9	1.7	2.5	2.9	2.60E+13	0.7	272	54	−45	NF	92	5	3
13	10 713	0101	8.42	37.744	15.002	0.4	−0.3	2.6	3.2	7.70E+13	0.6	251	26	−60	NF	42	34	24
14	10 713	0108	22.01	37.745	15.005	0.2	−0.8	2.3	2.7	1.10E+13	0.7	119	34	−163	NS	65	6	30
15	10 713	0201	48.34	37.747	15.008	−0.4	0.8	2.2	2.6	8.70E+12	0.7	108	43	175	SS	59	17	25
16	10 713	0204	3	37.718	15.012	2.1	2	2.2	2.9	2.10E+13	0.6	76	65	−13	SS	54	44	2
17	10 713	0208	20.25	37.745	15.006	−0.5		2.1	2.5	7.00E+12	0.6	330	78	−119	NS	54	15	31
18	10 713	0301	55.04	37.744	15.001	0.7	−0.5	2.6	3.1	4.30E+13	0.8	292	18	−68	NF	58	15	27
19	10 713	0402	30.78	37.745	15.001	0.9	0.8	2.6	3.2	8.20E+13	0.8	220	71	−109	NF	52	31	17
20	10 713	0136	45.34	37.716	15.038	1.2	1.4	2.9	3.2	7.90E+13	0.6	152	65	−14	SS	58	23	20
21	10 713	0201	35.41	37.719	15.009	1.2	1.7	2.5	2.7	1.10E+13	0.4	302	69	−115	NF	41	52	7
22	10 713	0313	33.21	37.706	15.043	0.9	2.8	3.5	3.5	1.90E+14	0.5	7	28	−116	NF	62	36	2
23	10 713	0324	40.67	37.718	15.009	0.7	1.6	3	2.8	1.60E+13	0.6	120	76	29	SS	57	22	22
24	10 713	0334	57.13	37.729	15.004	0.1	−0.1	2.6	2.6	7.80E+12	0.4	72	47	44	TF	58	34	8
25	10 713	0340	25.27	37.726	15.011	0.7	0.4	2.9	2.5	7.30E+12	0.6	71	81	33	SS	20	61	19
26	10 713	0345	13.55	37.707	15.042	1.5	2.0	2.7	2.8	2.00E+13	0.8	216	69	79	TF	7	64	29
27	10 713	0405	34.9	37.731	15.000	−0.1	−0.3	2.6	3.1	4.60E+13	0.7	338	69	−33	SS	42	32	26
28	10 713	0446	0.74	37.735	14.998	0.1	0.8	3.1	3	3.70E+13	0.6	26	88	57	UN	30	61	9
29	10 713	0449	45.23	37.713	15.041	2.3	3.1	2.6	3.3	9.80E+13	0.5	340	72	−175	SS	54	17	29
30	10 713	0456	16.37	37.737	14.995	0.3	−0.6	3.1	3	3.70E+13	0.5	195	51	88	TF	28	43	30
31	10 713	0511	47.74	37.737	15.001	−0.2	0.8	3.3	2.9	2.50E+13	0.5	51	81	65	UN	42	37	21
32	10 713	0549	31.34	37.710	15.036	1.5	2.4	2.9	3.1	4.90E+13	0.5	333	79	148	SS	9	77	15
33	10 713	0829	52.25	37.710	15.040	1.3	2.2	2.9	3.3	9.90E+13	0.8	346	56	−130	NF	90	2	8
34	10 713	0838	41.77	37.715	15.036	1.5	1.8	2.8	3.4	1.20E+14	0.9	220	60	−100	NF	22	51	27
35	10 713	1846	20.2	37.724	15.010	2.2	2.3	2.6	2.4	4.00E+12	0.5	333	81	−85	UN	69	12	20
36	10 713	1858	26.2	37.713	15.044	1.5	1.9	2.8	2.3	3.40E+12	0.6	253	75	162	SS	28	42	30
37	10 713	2116	44.84	37.733	15.006	1.0	1.2	2.7	2.6	8.90E+12	0.7	54	82	91	UN	48	32	20
38	10 713	2159	3.96	37.714	15.038	2.3	1.1	3	3.2	6.60E+13	0.6	243	80	−128	NS	96	3	1
39	10 713	2201	41.13	37.729	15.006	0.7	0.1	2.5	2.5	7.40E+12	0.5	300	72	−109	NF	72	23	5
40	10 713	2300	30.93	37.733	15.006	1.1	1.6	2.6	2.5	6.80E+12	0.7	177	18	−124	NF	33	44	23
41	10 714	0120	10.47	37.733	14.999	1.3		3	3.1	4.60E+13	0.6	239	63	126	TF	25	42	33
42	10 714	0854	8.75	37.713	15.038	1.5	1.8	3.5	3.2	6.70E+13	0.7	340	85	−164	SS	63	29	8
43	10 714	0906	50.81	37.706	15.039	1.2	2.4	2.6	2.6	7.80E+12	0.6	59	65	−9	SS	63	20	18
44	10 714	0914	54.43	37.713	15.029	1.4	2.5	2.6	2.5	6.50E+12	0.4	276	26	−150	NF	65	19	16
45	10 714	1002	32.53	37.736	15.002	1.3	2.2	2.3	2.5	7.30E+12	0.6	253	74	166	SS	20	67	13
46	10 714	1028	15.07	37.733	15.003	1.2	1.8	2.6	3	3.10E+13	0.6	150	58	−38	NS	42	51	6
47	10 714	1133	42	37.722	15.010	1.9	2.0	2.4	2.4	4.90E+12	0.4	358	51	−52	NF	76	5	20
48	10 714	1246	14.71	37.736	15.004	1.1	1.8	2.7	3	3.60E+13	0.5	285	72	−116	NF	62	19	19
49	10 714	1250	28.02	37.735	15.004	1.4	−0.5	2.8	1.8	5.80E+11	0.6	240	79	163	SS	85	6	9
50	10 714	1301	12.13	37.733	15.006	0.9	1.9	2.7	2.6	7.90E+12	0.5	240	3	100	UN	59	40	1
51	10 714	1343	50.68	37.707	15.041	1.1	0.9	2.8	2.7	1.30E+13	0.5	59	50	−34	NS	12	67	22
52	10 715	0457	30.77	37.701	15.042	0.5	1.1	3.4	3	3.30E+13	0.8	329	75	−36	SS	52	31	17
53	10 715	0457	48.19	37.707	15.043	0.7	1.7	3.5	3.4	1.60E+14	0.7	324	32	−111	NF	51	28	21
54	10 715	0459	39.67	37.705	15.040	1.0	1.2	2.8	2.1	1.70E+12	0.4	161	46	−174	UN	85	8	8
55	10 715	0702	54.15	37.734	15.002	−0.9	−0.5	2.9	2.3	3.70E+12	0.6	112	40	3	UN	38	42	20
56	10 715	0745	30.41	37.734	14.998	−0.4	−0.1	3.5	3.5	2.00E+14	0.4	309	82	155	SS	65	26	9
57	10 715	1018	2.24	37.707	15.039	0.3		2.9	2.4	3.80E+12	0.7	240	78	41	SS	27	44	29

technique when computing the base functions. When deriving moment tensors from short period data of local events, SH seismograms may augment the possibility of unstable inversion (Koch 1991), therefore we prefer to use only vertical components. If only vertical-component waveforms are used, a minimum of three stations is required to obtain the complete MTRFs (*P* and *SV* data for each station) (e.g. Panza & Saraò 2000). Nevertheless, even if the number of stations is sufficient, the inversion problem can be ill

Table 1. (*Continued.*)

N	Day	hhmm	ss.ss	Lat.	Long.	Depth	Depth MT	M_d	M_w	M_o (Nm)	Corr	Str	Dip	Rake	FPS type	DC per cent	CLVD per cent	V per cent
58	10 715	1034	36.92	37.712	15.039	−0.1	1.1	2.8	2.5	6.60E+12	0.7	183	72	87	TF	65	0	35
59	10 715	1226	58.54	37.733	14.999	−0.2	−0.4	2.6	2.3	3.00E+12	0.6	167	57	−27	NS	69	8	24
60	10 717	1340	19.12	37.710	15.004	−0.7	−0.3	3.3	3.1	4.60E+13	0.5	284	52	−69	NF	82	7	11
61	10 718	2000	59.08	37.708	15.006	−0.2		3	2.8	2.10E+13	0.7	239	64	18	SS	83	8	9

Note: We list the event number (N), the day (Day), hour, minutes (hhmm) and seconds (ss.ss), the hypocentral coordinates (Lat. Long., in degrees, and Depth b.s.l, in km), and the duration magnitude (M_d). The moment magnitude (M_w) computed from the seismic moment (M_o) through the Hanks & Kanamori relation (1979), the average correlation (Corr), strike (str), dip and rake of one nodal plane, the type of focal mechanism and the percentage of DC, CLVD and V are also reported. The type of focal mechanisms is classified according to Zoback (1992) criteria: NF, normal faulting; NS, predominately normal faulting with strike-slip component; SS, strike-slip faulting; TS, predominately thrust faulting with strike-slip component; UN, unclassified. The earthquakes 17, 41, 57 and 61 are poor quality inversion solutions and are not considered in the discussion.

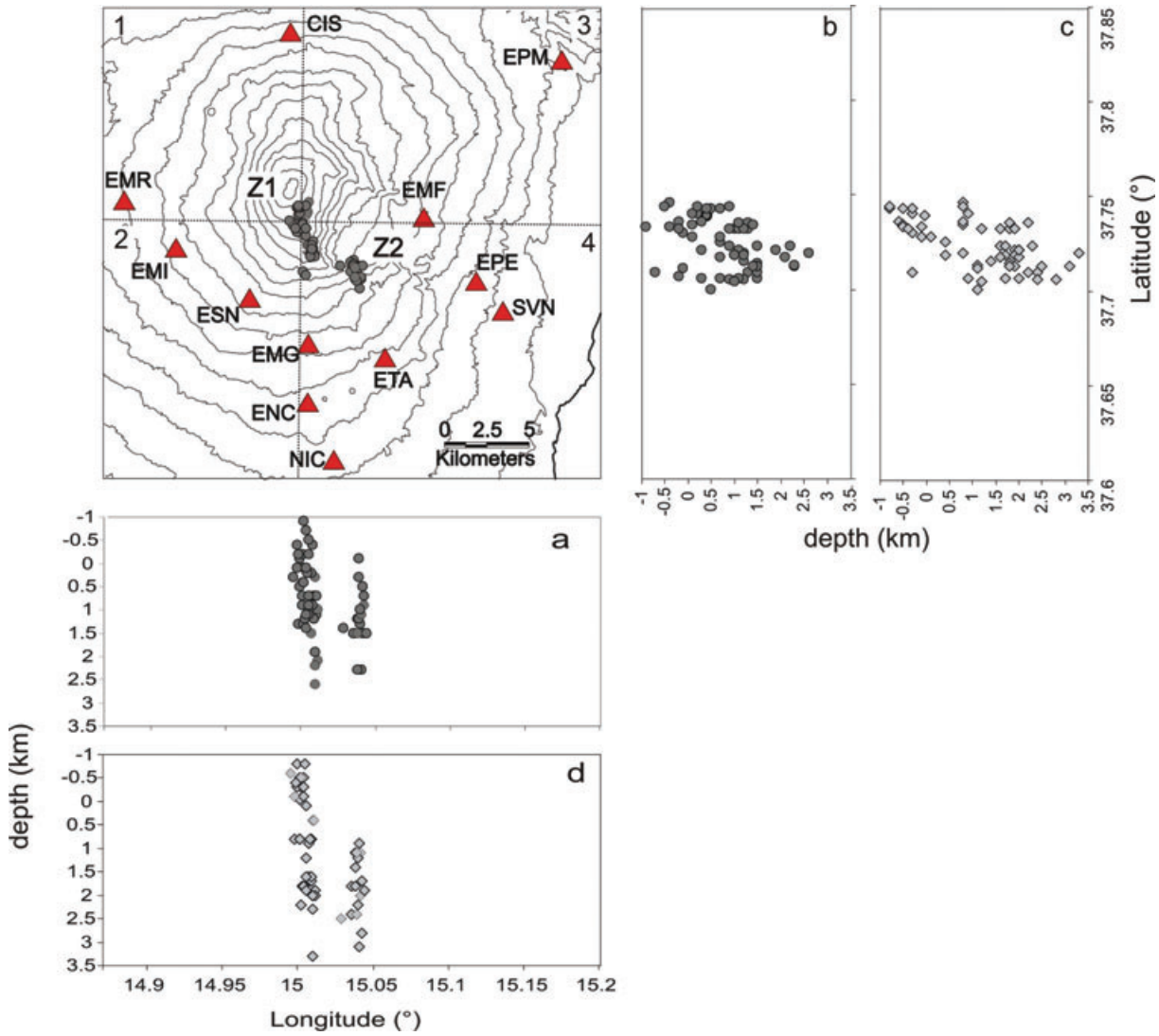

Figure 2. Epicentral map and vertical cross-sections of the earthquakes analysed. (a, b) Hypocentral depths obtained locating events with the 3-D velocity model; (c, d) the depths attained inverting MT. The stations considered in this study are plotted as triangles. Z1 and Z2 indicate the major and the minor cluster, respectively. The four sectors in which we subdivided the investigated area for the definition of the 1-D structural models are traced as well.

posed, so at least four signals, or more depending on the quality of the data, are used in each inversion.

In Fig. 3, we show examples of the recorded seismograms for two events (11 and 37 in Table 1) that are representative of the used data set. Before the inversion, the records are low-pass filtered with a corner frequency of 5 Hz to remove signals that may very likely be distorted by the complex crustal structure and anelastic attenuation. In previous studies (e.g. Saraò *et al.* 2001; Guidarelli *et al.* 2002, 2006; Foulger *et al.* 2004), this frequency band has been found suitable for data recorded by networks of short-period sensors like the one considered in this study (INGV-CT permanent seismic network). The *P*-wave polarities read from records with a clear first

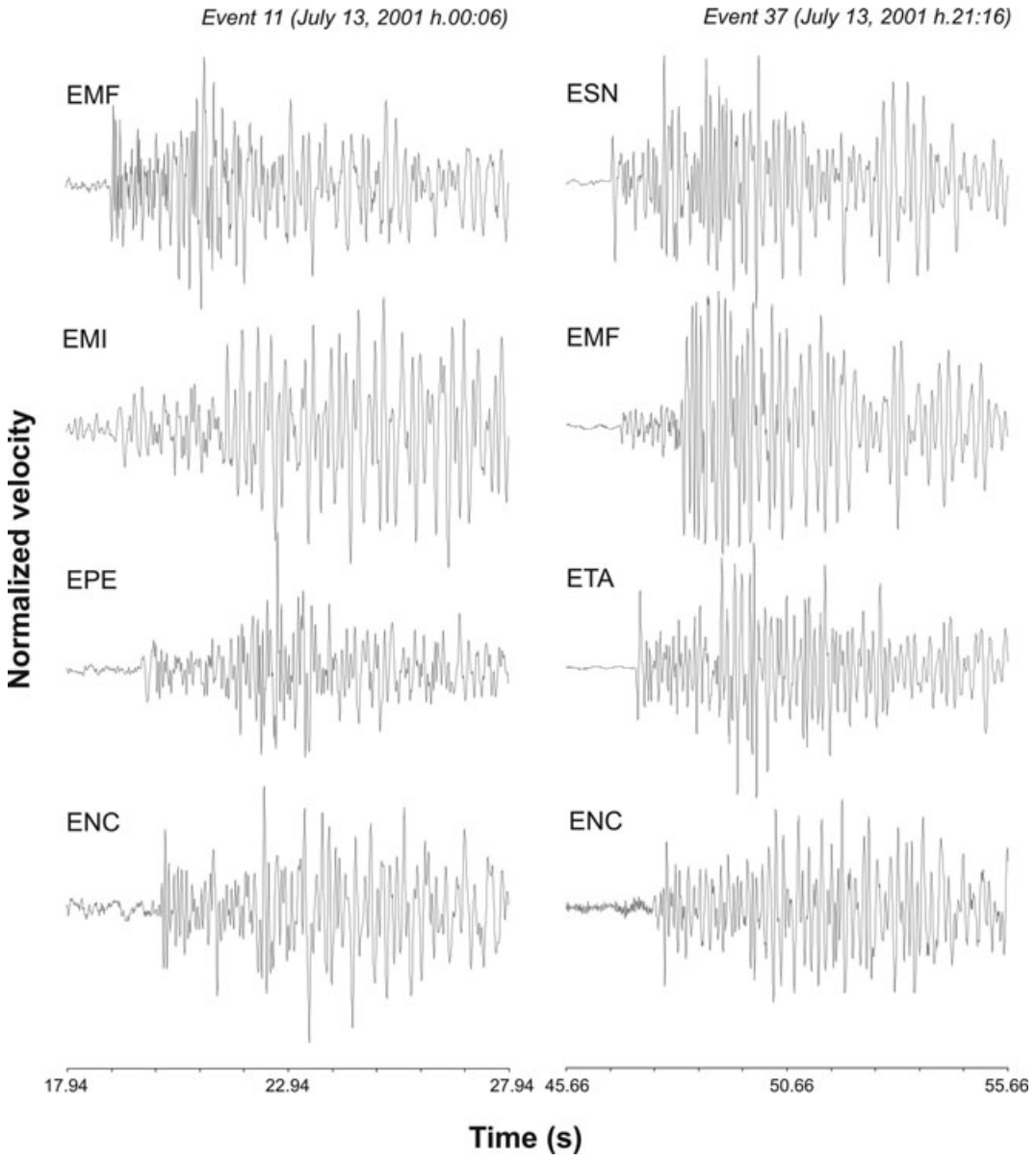

Figure 3. Examples of the recorded seismograms for two events (11 and 37 in Table 1) representative of the used data set.

arrival have been used as additional constraint in the second step of the moment tensor inversion.

The base functions, used to estimate the moment tensor by INPAR, have been computed using as extreme structural models those representing the recording and the hypocenter site, respectively. To obtain the different models, we subdivide the study area into four sectors (Fig. 2) and for each sector we extract an average 1-D velocity model from the 3-D model proposed by Patanè *et al.* (2006). The differences among the average 1-D models for the sectors 1, 2 and 3 are barely visible, therefore we computed the Green's functions only for two structural models, one (Fig. 4) representing the sectors 1, 2 and 3 (*etna_1*) and the other (Fig. 4) standing for sector 4 (*etna_4*). The structural model used for the epicentral area and for the recording site is chosen each time between these two, depending on the earthquake location and on the station position respectively. For each model, the density values are obtained from seismic velocities using the Nafe–Drake relation published by Ludwig *et al.* (1970) and the quality factor Q is defined in agreement with the attenuation tomography by Martinez-Arèvalo *et al.* (2005). The structural model used for the epicentral area and for the recording site is chosen each time between these two, depending on the earthquake location and on the station position, respectively.

4 RESULTS AND DISCUSSION

Most of the studied events were recorded during the early hours of the seismic swarm, starting from July 12 at 22:34 until July 18 at 00:20 and the selected data set reflects such earthquake distribution in time. To increase the stability of results, we have reduced the number of unknowns of the inversion problem by fixing the epicentre, obtained by the relocations with 3-D velocity models and have inverted only for the hypocentral depth and the six components of the moment tensor.

The depths obtained by moment tensor inversion (MT depths) derive from a search over a grid with 0.5 km step (Figs 2c and d). The

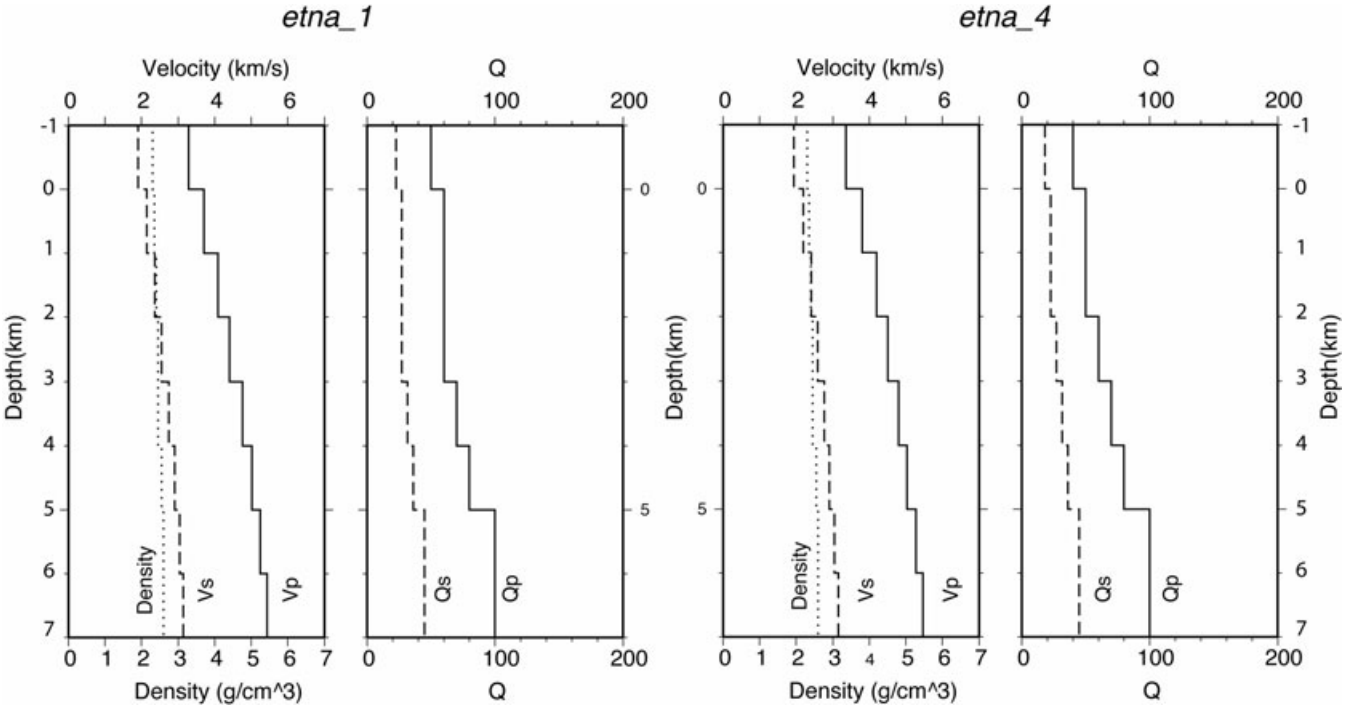

Figure 4. Average velocity, density and Q models used in this study. The structural model used for the epicentral area and for the recording site is chosen, for each inversion case, between these two depending on the earthquake location and on the station position, respectively.

comparison between the values of MT depths and the corresponding 3-D relocation depths (Table 1) show some small discrepancies (within 1 km) due to the dissimilar approaches and different data used. Nevertheless, the differences between the two distributions of depths are statistically significant at 80 per cent confidence level, as determined by the *Student t-test* (p-value = 0.2).

In Fig. 5, we show a selection of typical waveform fits obtained by inversion. Each panel corresponds to an earthquake numbered as in Table 1 and for each record used in the inversion, the correlation (ranging from 0 to 1) between the observed data and the modelled waveform is given.

The source mechanisms derived from the waveform inversion are plotted with the confidence areas of the moment tensor components (Fig. 6) using the Riedesel & Jordan (1989) representation. To be conservative, we discuss only events with confidence areas greater or equal to 90 per cent (Fig. 6); therefore solutions for events 17, 41, 57 and 61 are not considered in the following. Synthetic tests by Panza & Saraò (2000) and Saraò *et al.* (2001) prove that for the Etnean seismicity, low percentages of non-DC components—below 10 per cent for V and below 20 per cent for CLVD—cannot be reliably resolved.

Several authors (e.g. Foulger & Julian 1993; Panza & Saraò 2000) have shown that though complexities or anisotropy of the medium can introduce spurious CLVD in the solutions, a proper analysis of findings and the error analysis can help in discriminating between artefacts and physical solutions. On the other hand, when the temporal variation of the moment tensor is investigated, the relative variations in findings cannot be attributed to structure effects (ill-modelled structural features), because they do not change over the involved time scale (days), and the explanations of non-DC components must be sought in physical processes acting at the source. As an example we mention the events 11, 18 and 19 in Z1, sharing the same epicentral location and, within the error bars, the same depth, inverted using the same group of stations (Fig. 5) but having significantly different percentages of moment tensor components.

As already observed in many volcanic areas [e.g. at Hawaii (Thurber & Gripp 1988), Long Valley Caldera (Foulger *et al.* 2004)], different types of focal mechanisms are observed. Following the Zoback (1992) criteria based on the P, B and T-axes values, the focal mechanisms determined by our study (Fig. 7) can be classified as the following: 32 per cent of the fault plane solutions are of normal faulting type, 12 per cent are predominately of normal type with some strike-slip component, 30 per cent are strike-slip type, 9 per cent are of thrust faulting type and 17 per cent cannot be classified within the Zoback criteria. Such a picture is compatible with the complex local stress regime generated by the vertical dyke propagation and the tectonic stress field. Indeed, as proposed by Barberi *et al.* (2000) a North–South oriented vertical dyke induces a stress field able to surpass the regional one and producing a 90° rotation of the stress tensor.

We also computed fault plane solutions by inverting first-arrival polarities with FPFIT code (Reasenberg & Oppenheimer 1985). A straight comparison between the two sets of solutions is not meaningful, because, as is well known, the fault plane solutions determined with polarities are obtained in the DC source approximation. This is a rather strong constraint for volcano seismicity, where also small magnitude events can be generated by a complex interaction between fluids movements and local stress field, not referable to a simple double-couple assumption. We observe that the focal mechanisms determined from polarities and the moment tensor solutions are not comparable, for the events for which large V components and/or complex source time functions are observed. The agreement exists within the error areas, when the STF of the event, retrieved by INPAR, is simple. In the triangular parameterization (Nabelek 1984) adopted in our inversion method, simple means single-peaked, as the STF of events 4, 8, 9, 21 and 36 shown in Fig. 8. Multipeaked STFs might be associated to the fluid viscous damping at the crack

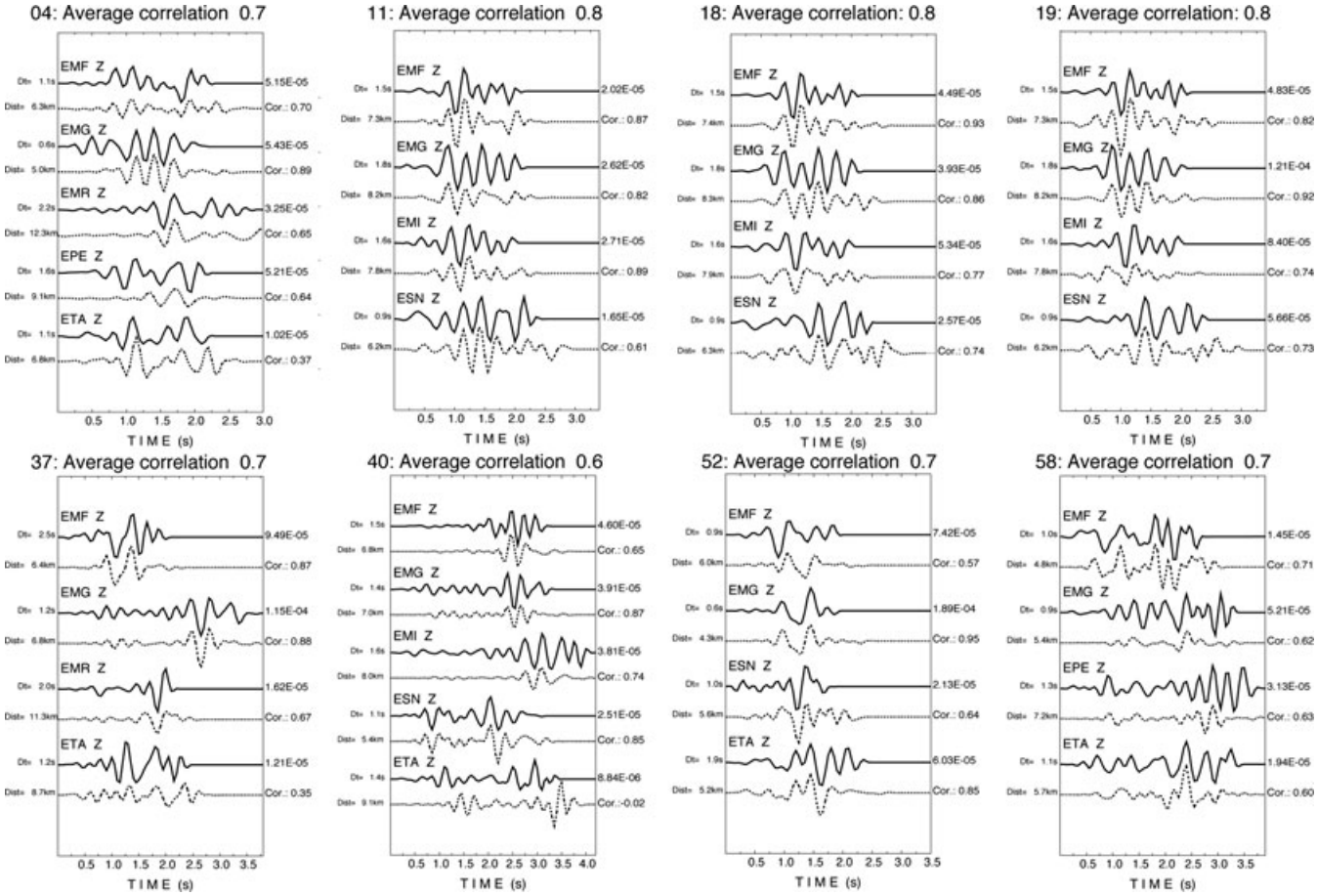

Figure 5. Examples of fit between recorded data (solid line) and synthetics (dotted line) for some events analysed in this study. Each panel number corresponds to the event number of Table 1. For each signal we report, on the left, the origin of the time window of the signal selected in the inversion and the epicentral distance, whilst the maximum amplitudes and the correlation value (Cor.) are given on the right.

wall (Chouet & Julian 1985) or to multiple events, but to unravel these possibilities is difficult because the STF can be very sensitive to biasing effects due to ill-modelled structural features and to wave scattering in complicated media (e.g. Sileny *et al.* 1996; Lokmer *et al.* 2007).

An overview of the distribution of the moment tensor components is given by the boxplot (Fig. 9a) and by the ternary diagram (Fig. 9b). Through the boxplot we represent the median (the bold line in the box), the lower and the upper quartile (lower and upper edge (hinge) of the box) and the minimum and maximum value (the ends of the vertical lines or "whiskers") of the solution data set. From this plot we observe that DC components are distributed around 56 per cent with maximum value of 92 per cent and minimum of 7.4 per cent, the CLVD components are distributed around 30 per cent with maximum values of 78 per cent and minimum 0 per cent, and that the V components are quite close, concentrated around 17 per cent with a maximum value of 35 per cent and minimum value of 0.8 per cent. By the ternary diagram (Fig. 9b) we have also detailed information about the percentage components for each event in both Z1 and Z2 sectors.

The DC percentage distribution indicates that most of the investigated seismicity may be due to tensile failure with simultaneous slip, perfectly compatible with fluid flow intrusion. In Z1 there are events with large DC components (greater than 60 per cent), whereas the largest CLVD values (greater than 60 per cent) are observed for the Z2 events (Fig. 9b).

The studied earthquake sequence starts in the northernmost part of the Z1 area (sector Z1a in Fig. 7) on July 12 at 22.34 (*event 1*), but it is immediately followed by the activation of the southernmost part of Z1, in a sector that we name Z1b, with earthquakes occurring between July 12, 22:50 (*event 2*) and July 18, 00:20 (*event 61*). On July 13, the seismic activity stops in Z1a (*event 19*), and a new sector, that we name Z1c, located between Z1a and Z1b (Fig. 7), becomes active (*event 24*).

In Fig. 10, we show a simplified cartoon, based on speculative interpretation, with the investigated seismicity as related to the dyke system. We represent the intrusions from the central feeding systems (Fig. 10a) separated from the up rising of eccentric dykes (Fig. 10b). The earliest events of the three sectors are shallow, although the hypocenters of Z1b are, in general, deeper than in Z1a and Z1c (Figs 10a and b).

The shallowest earthquakes are located where fissures can easily develop, due to the dominance of the tensile stress over the lithostatic pressure, mainly if the medium is pre-fractured.

A scatter plot (Fig. 11) shows the temporal variation of moment tensor components. The early events have DC components greater than 70 per cent, both in sectors Z1a and Z1b (Fig. 11a) that decrease until *event 31* in Z1c and *event 25* in Z1b respectively and seem to increase again as the eruption approaches. Such DC variations are more evident in the boxplots (Figs 12a and b) obtained after grouping the seismicity into three subsets for both sector Z1ac and Z1b.

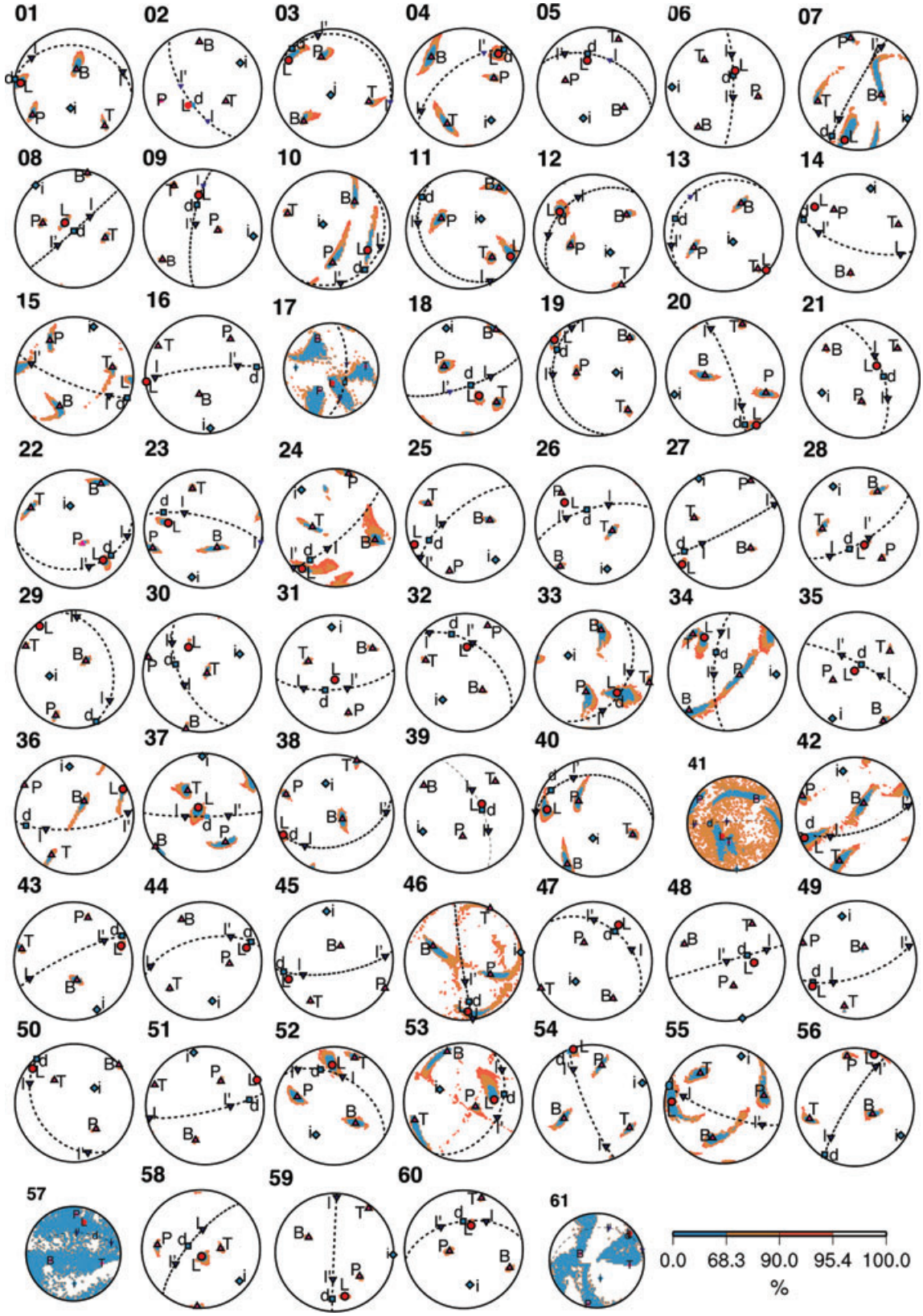

Figure 6. Complete source mechanisms, with confidence error ellipses, represented following Riedesel-Jordan (1989) formalism. **L** is the vector describing the total mechanism, **d** is the DC vector, **l** and **l'** are the CLVD with major dipole along the tensional and the pressure axes, respectively. **i** represents a pure *V*; T, P and B indicate the tensional, compression and null axes, respectively. Triangles pointing downwards are vectors in the lower hemisphere, triangles pointing upwards are vectors on the upper hemisphere. Hatched areas around the L, P, T and B axes are the projections of the confidence areas onto the focal sphere. The distance of **L** from the vectors **I**, **d**, **l** and **l'** displays the share of *V*, DC and CLVD components, respectively. Events 17, 41, 57 and 61 show very large error areas and are not considered in the discussion.

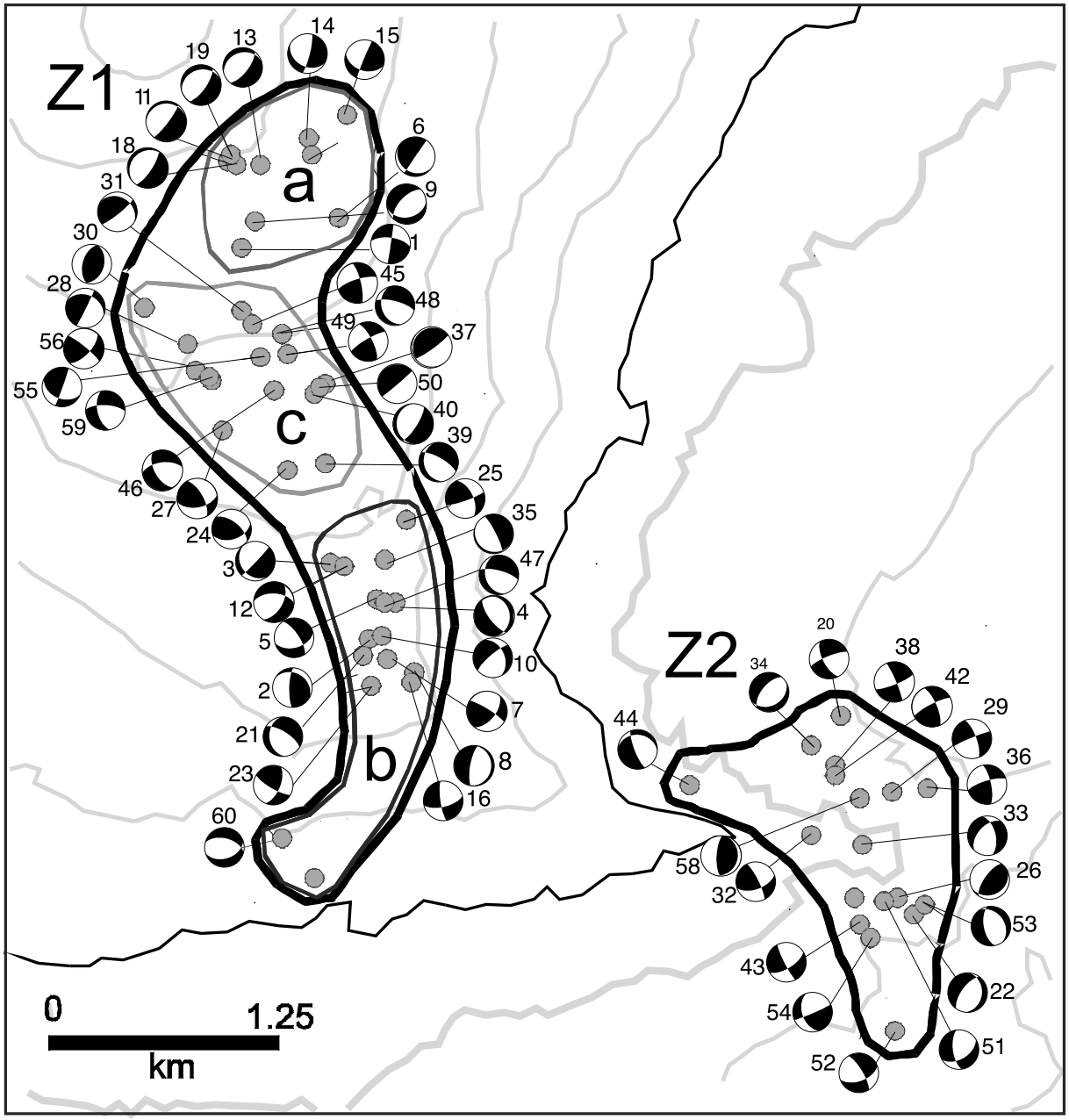

Figure 7. Focal mechanisms (best double-couple) obtained from moment tensor inversion (INPAR) in this study. Z1 (a–c) and Z2 sectors correspond to spatio-temporal grouping of the investigated seismicity.

The *Student t-test* reveals that the DC variation between Z1ac1 and Z1ac2 is statistically significant at 95 per cent confidence level (p-value = 0.04); the variation between Z1b1 and Z1b2 is statistically significant at 90 per cent confidence level (p-value = 0.10); the variations observed between Z1ac2 and Z1ac3 (p-value = 0.3) as well as Z1b2 and Z1b3 (*p-value = 0.2*) are not statistically significant at 95 per cent confidence level.

The *Kendall's tau* statistics, that measures the strength of the relationship between two variables, gives a negative correlation (i.e. decreasing trend) for both the subsets and therefore validates that the DC decrement observed between Z1ac1–Z1ac2 and Z1b1–Z1b2 is statistically significant at 95 and 90 per cent, respectively.

The decrement of DC in favour of non-DC increment in sectors Z1ac and Z1b is likely due to fluid dynamics phenomena since after the opening of the first fissures system, the magma intrusion process is facilitated.

The earthquake sources compatible with intrusion (CLVD > 60 per cent) are found at relatively greater depths (Figs 10a and b) in agreement with other geophysical evidences.

The variations observed between Z1ac2 and Z1ac3 as well as Z1b2 and Z1b3 are not statistically significant at 95 per cent confidence level and this can be due to the temporal data distribution; indeed, although in Z1ac1–Z1ac2 and Z1b1–Z1b2 data are very closely distributed in time within the early hours after the beginning of the seismic swarm, the third subsets contain earthquakes spanning the leftover time before the eruption (5 days) and probably refer to different phases of the volcano dynamics preceding the eruption. Probably an increase of the number of data for these subsets would

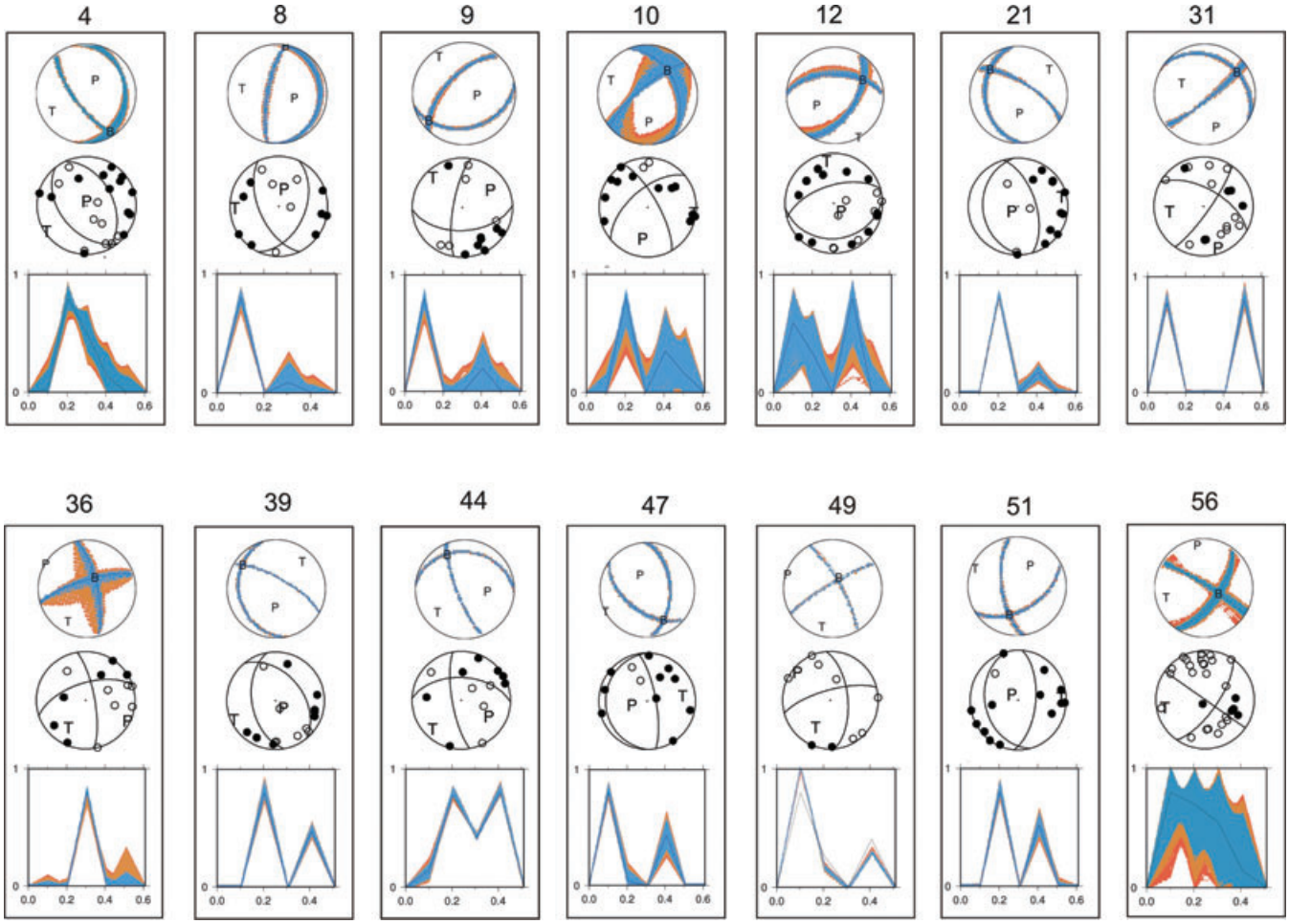

Figure 8. Comparison between a selection of focal mechanisms (best double-couple) retrieved by INPAR and fault plane solutions determined by first arrivals polarity. For each panel: the number identifies the earthquake listed in Table 1; the first and the third row show the focal mechanism (best double-couple) and the source time function obtained by INPAR and the second row gives the fault plane solution as obtained by polarities. The colour legend is the same as for Fig. 6.

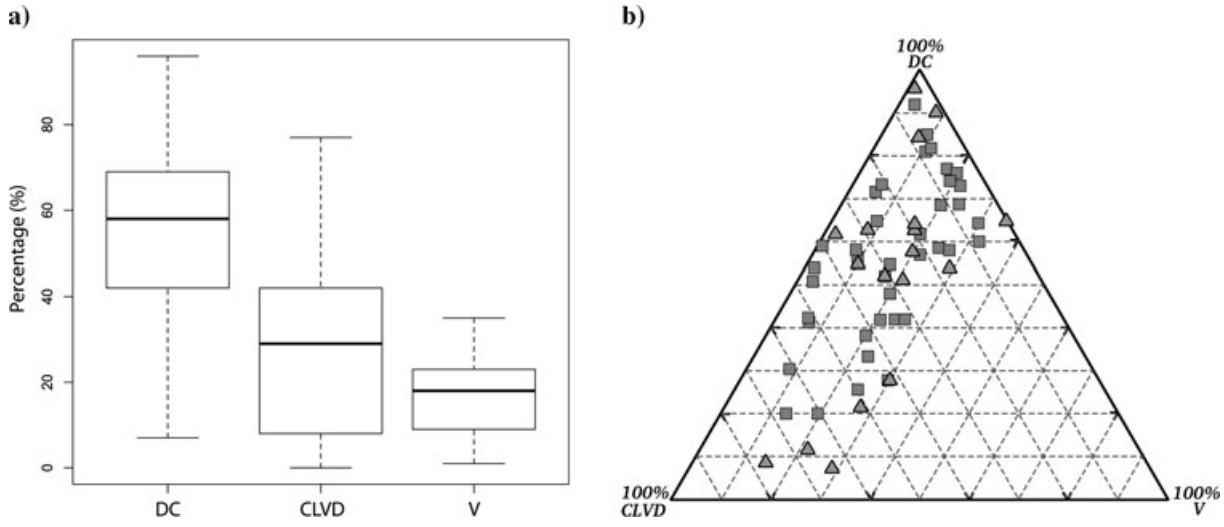

Figure 9. (a) Boxplot for the percentage of moment tensor component, DC, CLVD and V. The upper and lower ends of the box are drawn at the quartiles, and the bar through the box is drawn at the median. The whiskers extend from the quartiles to the maximum and minimum data values. The box itself contains the middle 50 per cent of the data. If the median line is not equidistant from the hinges, then data are asymmetrically distributed. (b) Ternary diagram showing the percentage of DC, CLVD and V retrieved for the earthquakes located in Z1 (squares) and Z2 (triangles).

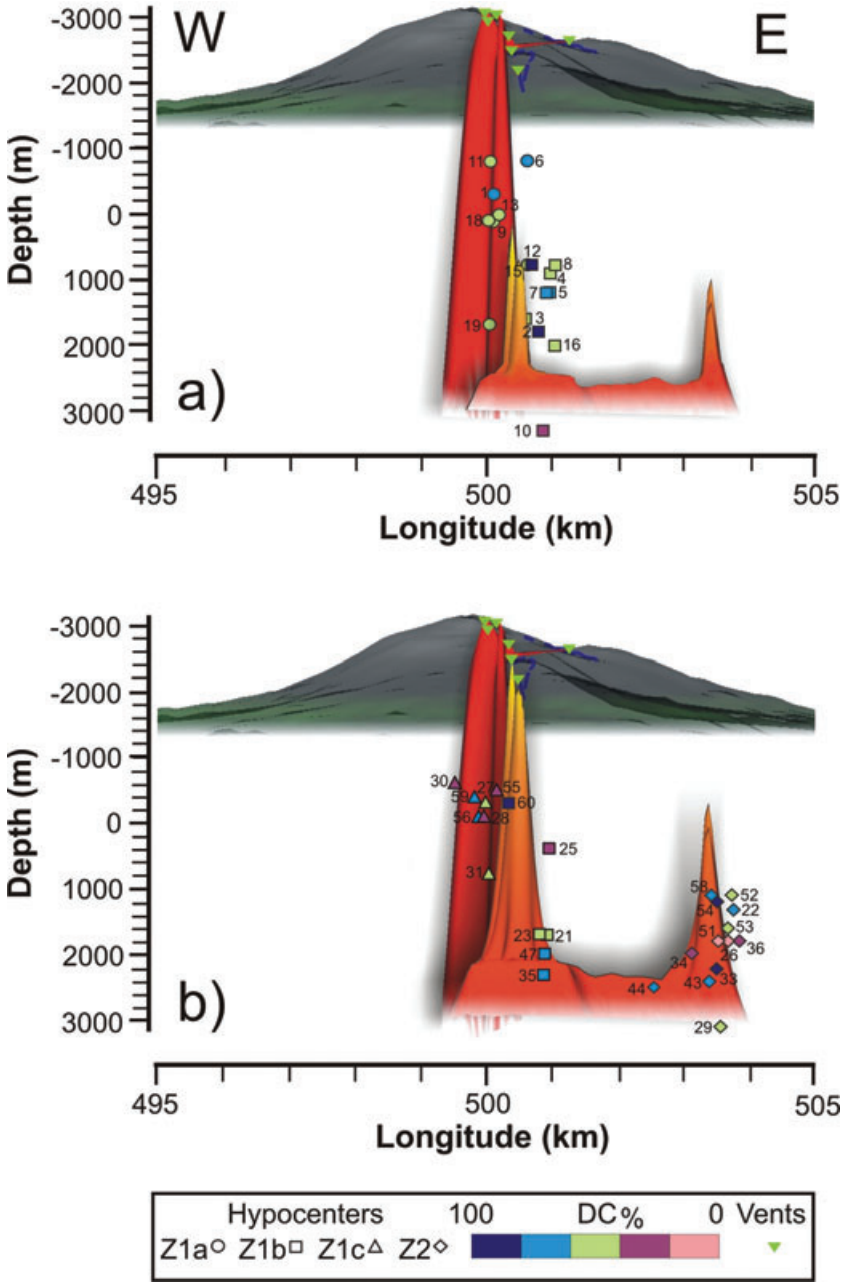

Figure 10. Speculative model of the central feeding system (red) and evolution of eccentric dykes (orange and yellow) during the analysed period (2001 July 12–18). Intrusions from the central feeding system (a) precede the rise of eccentric dykes (b). Seismicity is plotted with different symbols for each of the identified zones with colours that represent the DC component percentages. The numbers are associated with earthquakes listed in Table 1; events located beyond eccentric dykes are not shown. The fracture system (blue lines) and eruptive vents are also reported.

statistically validate what we glimpse from the boxplot, that is an increment of DC percentage going towards the eruption, that could be explained as the brittle response of the confining medium to the stress regime induced by the dyke emplacement. Such a picture would be compatible with the stress regime model for a dyke injection, as proposed by Bonafede & Danesi (1997).

The sequence in the Z2 area starts on July 13 at 01:36 (*event 20*) and ends on July 15 (*event 58*). The average depth of the seismicity occurring on July 13 and 14 is about 1.5 km with hypocenters located between 0 and 3 km (Fig. 10b). The events occurring on July 15 (from *event 52*) are shallower than the earlier ones. During this interval, we observe a combination of DC and non-DC events (Fig. 11b) with some large CLVD component (77 per cent) but also events with DC components greater than 80 per cent. As shown by the boxplot of Fig. 12b, where we group the seismicity following similar criteria as for Z1ac and Z1b, the data are not symmetrically distributed around the medians and the *Student's t-test* confirms that the observed variations are not statistically significant at 95 per cent confidence level.

The absence of any peculiar feature can be seen as representative of a still immature process of magma reclimbing which did not lead to the eruption, since the magma stopped at around the sea level, where it lost the pressure necessary to overcome the lithostatic load. The hypothesis of an aborted eruption, which is not excluded by

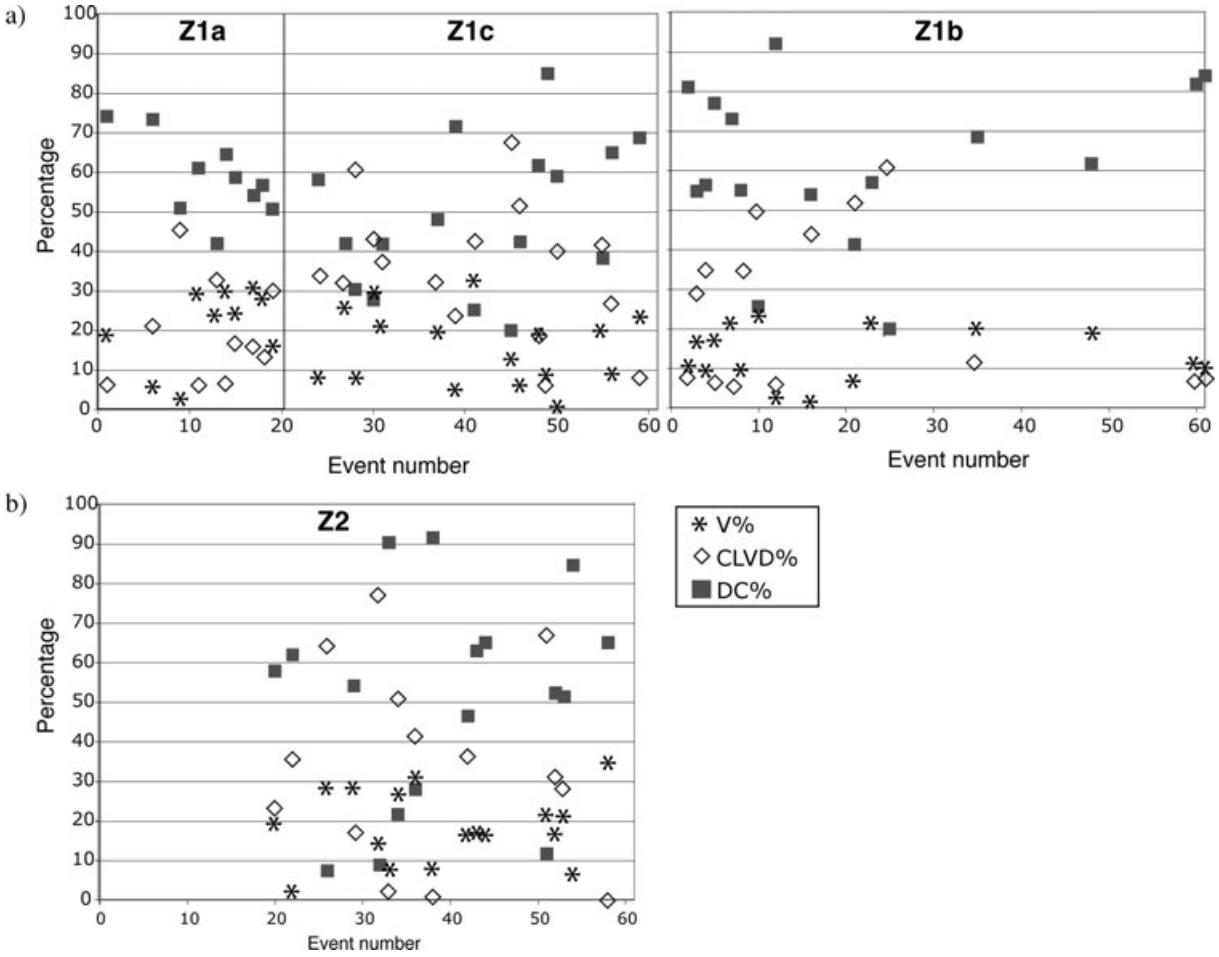

Figure 11. (a) Temporal variation of the three moment tensor components in the subsectors Z1a, Z1c and Z1b. (b) Temporal variation of the three moment tensor components in Z2.

Musumeci *et al.* (2004), is supported by several other geophysical observations. In particular, high V_p anomaly in the velocity structure (Patanè *et al.* 2002), low Q_p (Martinez-Arevalo *et al.* 2005) and negative gravity anomaly (Carbone *et al.* 2003) have been observed in the sector Z2. Moreover, ground deformations observed by GPS (Bonforte *et al.* 2004) show a pattern compatible with a dyke intrusion, and extensometer data (Gambino 2004) collected slightly east of Z2, highlight ground movements that are in agreement with the mechanism proposed here.

5 CONCLUSION

The analysis of 61 earthquakes occurring before the 2001 July eruption provides new insights into the eruptive processes at Mt. Etna. The source moment tensors retrieved show different kinds of focal mechanisms with a predominance of normal faulting (44 per cent) and a few strike slip (30 per cent) and thrust mechanisms (9 per cent), all of them compatible with the complex local stress regime generated by vertical dyke propagation.

The focal mechanisms determined from polarities and INPAR are comparable, within the error areas, for the events with relatively small V components (less than 25 per cent) and simple STF.

The northern part of the 2001 eruptive phenomenon is seismically active only for a few hours during the first stage of the swarm (Z1a) with a high percentage of DC components (greater than 70 per cent). At the same time, the deeper portion of Z1b is affected by earthquakes (located 1.0–2.5 km b.s.l.) with significant percentage of CLVD components (20–50 per cent). After 4 hr, the seismic activity stops in Z1a and starts in Z1c, where earthquakes with a significant CLVD component (30–60 per cent) occur as well. The DC variation observed in the early hours in both sectors Z1ac and Z1b are statistically significant at 95 and 90 per cent confidence levels, respectively. In our opinion, after the opening of the first fissures system, the magma intrusive process is facilitated. Then the percentage of non-DC earthquakes increases until, proceeding towards the onset of the eruption, the stress regime imposed by the dyke emplacement dominates again and DC events could occur mostly as brittle response of the confining medium. The intrusion of the primitive batch of magma starts in Z1b, at a depth of 2–3 km, aligned along the early surface fractures. The fracture system develops towards north and intersects, on July 17, the highly fractured zone (Z1a) where old batches of magma were residing (Corsaro *et al*. 2007). The intrusion started in Z1b, reaches the surface on July 18 and outpours gas-rich magma with primitive composition and basement xenoliths (Corsaro *et al*. 2007), testifying to a high-velocity uprising dyke.

The sequence in Z2 area starts later, on July 13, and the maximum depth of hypocenters is comparable to that of Z1. A still immature process of magma reclimbing can explain the erratic variation of observed DC percentage, not statistically significant at 95 per cent confidence level. These features, together with the trend of the focal

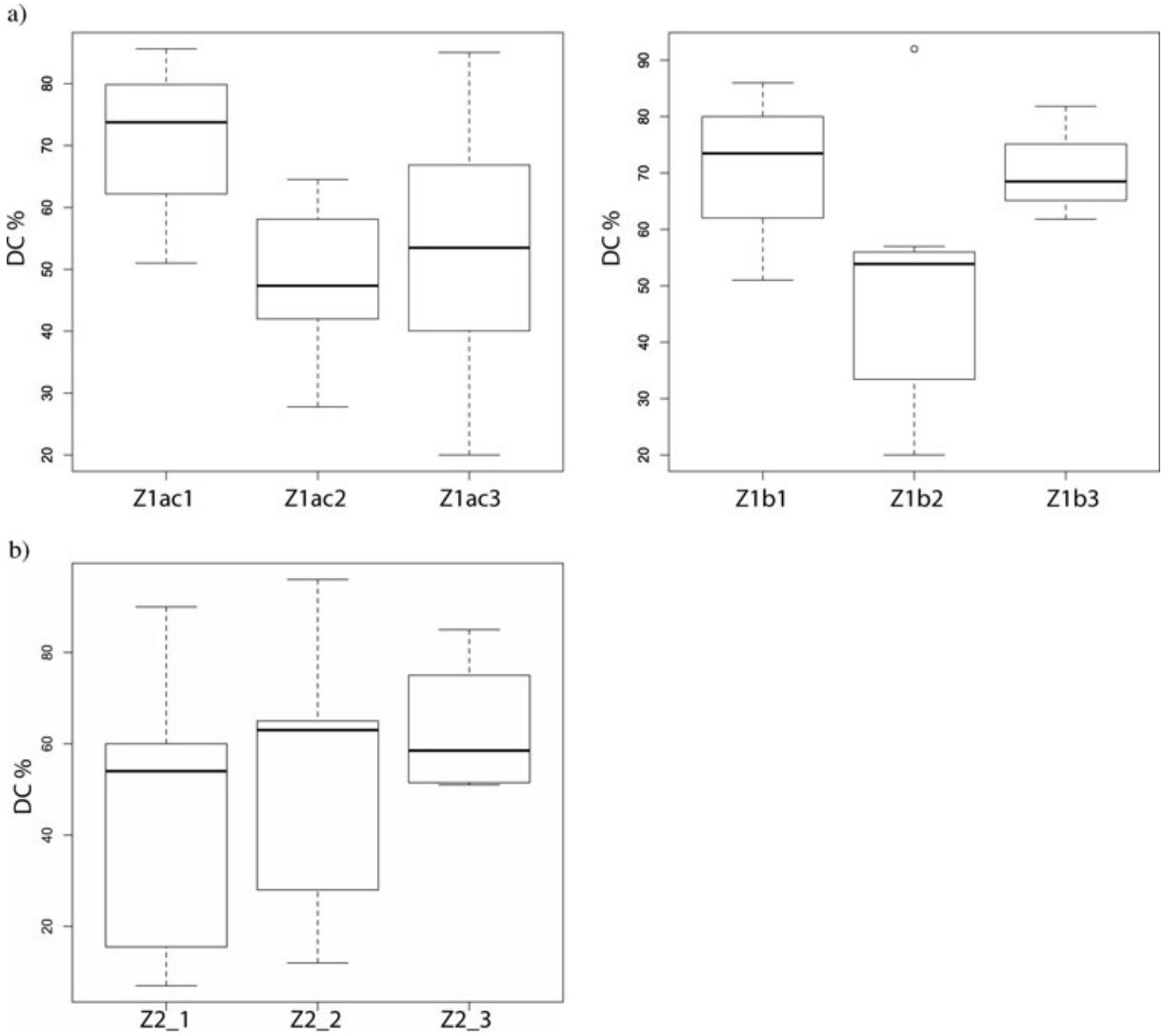

Figure 12. (a) Boxplot of the DC percentage of moment tensor component in the subset Z1ac1 (events 1, 6, 9, 11), Z1ac2 (events 13, 14, 15, 18, 19, 24, 27, 28, 30, 31), Z1ac3 (events 1, 37, 39, 45, 46, 48, 49, 50, 55, 56, 59) and Z1b1 (events 2, 3, 4, 5, 7), Z1b2 (events 2,8, 10, 12, 16, 21, 23, 25), Z1b3 (events 35, 48, 60). (b) Boxplot of the DC percentage of moment tensor component in Z2_1 (events 20, 22, 26, 29, 32, 33, 34), Z2_2 (events 36, 38, 42, 43, 44, 51), and Z2_3 (event 52, 53, 54, 58).

depths, suggest a magma intrusion parallel to that occurring under Z1b that is tentatively associated with the same magma reservoir, which fed the lowermost part of the 2001 fracture system. The intrusion stops at around the sea level, where it loses the necessary pressure to overcome the lithostatic load.

ACKNOWLEDGMENTS

The authors thank Martha Savage and the Editor Yehuda Ben-Zion for their suggestions and valuable comments that helped in greatly improving the paper. Antonella Peresan is acknowledged for useful discussions on statistics.

REFERENCES

Aiuppa, A., Federico, C., Paonita, A., Pecoraino, G. & Valenza, M., 2002. S, C1 and F degassing as an indicator of volcanic dynamics: the 2001 eruption of Mount Etna, *Geophys. Res. Lett.,* **29,** doi: 10.1029/2002GL015032.

Alparone, S., Andronico, D., Giammanco, S. & Lodato L., 2004. A multidisciplinary approach to detect active pathways for magma migration and eruption at Mt. Etna (Sicily, Italy) before the 2001 and 2002–2003 eruptions, *J. Volc. Geotherm. Res.,* **136,** 121–140.

Barberi, G., Cocina, O., Neri, G., Privitera, E. & Spampinato, S., 2000. Volcanological inferences from seismic strain tensor computation at Mt. Etna Volcano, Sicily, *Bull. Volcanol.,* **62,** 318–330.

Behncke, B. & Neri, M., 2003. The 2001 eruption of Mt. Etna (Sicily), *Bull. Volcanol.,* **63,** doi: 10.1007/s00445-003-0274-1.

Bonaccorso, A., Aloisi, M. & Mattia, M., 2002. Dike emplacement forerunning the Etna July 2001 eruption modeled through continuous tilt and GPS data, *Geophys. Res. Lett.,* **29,** doi: 10.1029/2001GL014397.

Bonaccorso, A., D'Amico, S., Mattia, M. & Patanè, D., 2004. Intrusive mechanisms at Mt. Etna forerunning the July-August 2001 eruption from seismic and ground deformation data, *Pure appl. Geophys.,* **161,** 1469–1487, doi: 10.1007/s00024-004-2515-4.

Bonafede, M. & Danesi, S., 1997. Near-field modifications of stress induced by dyke injection at shallow depth, *Geophys. J. Int.,* **130,** 435–448.

Bonforte, A., Guglielmino, F., Palano, M. & Puglisi, G., 2004. A syn-eruptive ground deformation episode measured by GPS, during the 2001 eruption on the upper southern flank of Mt Etna, *Bull. Volc.,* **66,** 366–341.

Carbone, D., Budetta, G., Greco, F. & Rymer, H., 2003. Combined discrete and continuous gravity observations at Mount Etna, *J. Volc. Geotherm. Res.,* **123,** 123–135.

Chouet, B.A. & Julian, B.R., 1985. Dynamics of an expanding fluid-filled crack, *J. geophys. Res.,* **90,** 11 187–11 198.

Corsaro, R.A., Miraglia, L. & Pompilio, M., 2007. Petrologic evidence of a complex plumbing system feeding the July–August 2001 eruption of Mt. Etna, Sicily, Italy, *Bull. Volc.,* **69,** 401–421, doi: 10.1007/s00445-006-0083-4.

Foulger, G.R. & Julian, B.R., 1993. Non-double couple earthquakes at the Hengill-Grensdalur Volcanic Complex, Iceland: are they the artifacts of crustal heterogeneity?, *Bull. seismol. Soc. Am.,* **83,** 38–52.

Foulger, G.R., Julian, B.R., Hill, D.P., Pitt, A.M., Malin, P.E. & Shalev, E., 2004. Non-double-couple microearthquakes at Long Valley caldera, California, provide evidence for hydraulic fracturing, *J. Volc. Geotherm. Res.,* **132,** 45–71.

Gambino, S., 2004. Continuous dynamic response along a pre-existing structural discontinuity induced by the 2001 eruption at Mt. Etna, *Earth Planets Space,* **56,** 447–456.

Guidarelli, M. & Panza, G.F., 2006. Determination of the seismic moment tensor for local events in the South Shetland Islands and Bransfield Strait, *Geophys. J. Int.,* **167,** 684–692, doi: 10.1111/j.1365-246X.2006.02953.x.

Guidarelli, M., Saraò, A. & Panza, G.F., 2002. Surface wave tomography and seismic source studies at Campi Flegrei (Italy), *Phys. Earth planet. Int.,* **134,** 157–173.

Guidarelli, M., Zille, A., Saraò, A., Natale, M., Nunziata, C. & Panza, G.F., 2006. Shear-wave velocity models and seismic sources in Campanian volcanic areas: Vesuvio and Campi Flegrei, in *Vesuvius 2000: Education, Security and Prosperity,* pp. 287–309, ed. Dobran, F., Elsevier, Amsterdam.

Hanks, T.C. & Kanamori, H., 1979. A moment magnitude scale, *J. geophys. Res.,* **84,** 2348–2350.

INGV- Sezione di Catania, 2001. Multidisciplinary approach yields insights into Mt. Etna eruption, *EOS Trans. Am. geophys. Un.,* **85/52,** F653.

Jost, M.L. & Herrmann, R.B., 1989. A student's guide to and review of moment tensors, *Seismol. Res. Lett.,* **60,** 37–57.

Kravanja, S., Panza, G.F. & Sileny, J., 1999. Robust retrieval of seismic point source time function, *Geophys. J. Int.,* **136,** 385–394.

Koch, K., 1991. Moment tensor inversion of local earthquake data – I. Investigation of the method and its numerical stability with model calculations, *Geophys. J. Int.,* **106,** 305–319.

Lahr, J.C., 1989. HYPOELLIPSE/VERSION 2.0*: a computer program for determining local earthquake hypocentral parameters, magnitude, and first motion pattern,U.S. Geological Survey Open-File Report **89/116,** 81 pp.

Lokmer, I., Bean, C.J., Saccorotti, G. & Patanè, D., 2007. Moment-tensor inversion of LP events recorded on Etna in 2004 using constraints obtained from wave simulation tests, *Geophys. Res. Lett.,* **34,** L22316, doi: 10.1029/2007GL031902.

Ludwig, W.J., Nafe, J.E. & Drake, C.L., 1970. Seismic refraction, in *The Sea,* vol.4, pp. 53–84, ed. Maxwell, A.E., Wiley-Interscience, New York.

Martínez-Arévalo, C., Patanè, D., Rietbrock, A. & Ibáñez, J.M., 2005. The intrusive process leading to the Mt. Etna 2001 flank eruption: constraints from 3-D attenuation tomography, *Geophys. Res. Lett.,* **32,** L21309. doi: 10.1029/2005GL023736.

Musumeci, C., Cocina, O., De Gori, P. & Patanè, D., 2004. Seismological evidence of stress induced by dike injection during the 2001 Mt. Etna eruption, *Geophys. Res. Lett.,* **31,** L07617, doi: 10.1029/2003GL019367.

Nabelek, J.L., 1984. Determination of earthquake parameters from inversion of body waves, *PhD thesis*. Massachusetts Institute of Technology, Cambridge, USA.

Panza, G.F., 1985. Synthetic seismograms: the Rayleigh waves modal summation, *J. Geophys.,* **58,** 125–145.

Panza, G.F. & Saraò, A., 2000. Monitoring volcanic and geothermal areas by full seismic moment tensor inversion: are non-double couple components always artefacts of modelling?, *Geophys. J. Int.,* **143,** 353–364.

Panza G.F., Romanelli, F. & Vaccari, F., 2000. Seismic wave propagation in laterally heterogeneous anelastic media: theory and applications to seismic zonation, *Adv. Geophys.,* **43,** 1–95.

Patanè, D., Chiarabba, C., Cocina, O., De Gori, P., Moretti, M. & Boschi, E., 2002. Tomographic images and 3D earthquake locations of the seismic swarm preceding the 2001 Mt. Etna eruption: evidence for a dyke intrusion, *Geophys. Res. Lett.,* **29,** 1497, doi: 10.1029/2001GL014391.

Patanè, D. *et al.,* 2003. Seismological constraints for the dike emplacement of July-August 2001 lateral eruption Mt. Etna volcano, Italy, *Ann. Geophys.,* **46,** 599–608.

Patanè, D., Barberi, G., Cocina, O., De Gori, P. & Chiarabba, C., 2006. Time-resolved seismic tomography detects magma intrusions at Mount Etna, *Science,* **313,** 821–823.

Riedesel, M.A. & Jordan, T.H., 1989. Display and assessment of seismic moment tensors, *Bull. seismol. Soc. Am.,* **79,** 85–100.

Reasenberg, P.A. & Oppenheimer, D., 1985. FPFIT, FPPLOT AND FPPAGE: fortran computer programs for calculating and displaying earthquake fault-plane solutions,U.S. Geological Survey Open-File Report, 85–739.

Saraò, A., Panza, G.F., Privitera, E. & Cocina, O., 2001. Non double couple mechanisms in the seismicity preceding 1991–1993 Etna volcano eruption, *Geophys. J. Int.,* **145,** 319–335.

Šílený, J., 1998. Earthquake source parameters and their confidence regions by a genetic algorithm with a "memory", *Geophys. J. Int.,* **134,** 228–242.

Šílený, J. & Panza, G.F., 1991. Inversion of seismograms to determine simultaneously the moment tensor components and source time function for a point source buried in a horizontally layered medium, *Stud. geophys. Geod.,* **35,** 166–183.

Šílený, J., Panza, G.F. & Campus, P., 1992. Waveform inversion for point source moment tensor retrieval with optimization of hypocentral depth and structural model, *Geophys. J. Int.,* **108,** 259–274.

Šílený J., Campus, P. & Panza, G.F., 1996. Seismic moment tensor resolution by waveform inversion of a few local noisy records–I. Synthetic tests, *Geophys. J. Int.,* **126,** 605–619.

Silver, P.G. & Jordan, T.H., 1982. Optimal estimation of scalar seismic moment, *Geophys. J. R. astr. Soc.,* **70,** 755–787.

Thurber, C.H., 1993. Local earthquake tomography: velocity and Vp/Vs-theory, in *Seismic Tomography: Theory and Practice,* pp. 563–583, eds. Iyer, H.M., Hirahara, K., Chapman and Hall, London.

Thurber, C. & Gripp, E., 1988. Flexure and seismicity beneath the south flank of Kilauea volcano and tectonic implications, *J. geophys. Res.,* **93,** 4271–4278.

Zoback, M.L., 1992. First- and second-order patterns of stress in the lithosphere: the world stress map project, *J. geophys. Res.* **97,** 11 703–11 728.